Volume 13 | Number 42 | 14 November 2017 | Pages 7691–7814

Soft Matter

rsc.li/soft-matter-journal

ISSN 1744-6848

ROYAL SOCIETY OF CHEMISTRY

PAPER
Qiming Wang *et al.*
Stretchable 3D lattice conductors

Soft Matter

PAPER

View Article Online
View Journal | View Issue

Cite this: *Soft Matter*, 2017, **13**, 7731

Received 19th July 2017,
Accepted 19th September 2017

DOI: 10.1039/c7sm01435j

rsc.li/soft-matter-journal

Stretchable 3D lattice conductors†

Tingyao Li, Yanhui Jiang, Kunhao Yu and Qiming Wang *

3D architectures have been long harnessed to create lightweight yet strong cellular materials; however, the study regarding how 3D architectures facilitate the design of soft materials is at the incipient stage. Here, we demonstrate that 3D architectures can greatly facilitate the design of an intrinsically stretchable lattice conductor. We show that 3D architectures can be harnessed to enhance the overall stretchability of the soft conductors, reduce the effective density, enable resistive sensing of the large deformation of curved solids, and improve monitoring of a wastewater stream. Theoretical models are developed to understand the mechanical and conductive behaviors of the lattice conductor. We expect this type of lattice conductors can potentially inspire various designs of 3D-architected electronics for diverse applications from healthcare devices to soft robotics.

1. Introduction

It is well known that 3D architectures can greatly facilitate the design of rigid materials to create lightweight yet strong cellular materials for diverse engineering applications ranging from structural panels, flow cooling, to energy absorption.[1–4] The underlying science stems from the fundamental relationships between the material stiffness/strength or internal surface area and the material density, usually characterized *via* Ashby charts.[1–4] Despite the prosperous studies on the 3D-architected rigid materials, the effects of 3D architectures on the soft materials have been less studied.[5,6]

Here, we focus on the effects of 3D architectures on soft stretchable electronics. A number of seminal strategies have been proposed to design stretchable electronics;[7–10] however, they are usually limited to either bulk shapes with high densities or 2D thin-film geometries. Whereas 3D-architected electronics have been fabricated for intriguing applications from neuron electrodes to foldable batteries,[11–21] most of these paradigms involve rigid conductors integrated with soft substrates. The rigid conductors in these 3D-architected electronics may induce limited stretchability or integration mismatch.[22–24] As a promising alternative, conductors with intrinsically-stretchable materials such as gels[25–30] and conductive polymer composites[31,32] have been recently proposed. Despite their great potential, processing these intrinsically-stretchable conductors into 3D complex architectures is still a long-lasting challenge.[5,24] Although Hong *et al.* showed the feasibility of 3D printing of stretchable hydrogels with the direct-writing method,[33] the 3D architectures with suspending beams are still challenging due to the requirement of self-weight supporting during the direct-writing process, thus limiting the overall architecture choices.[5,6,33]

In this report, we present a strategy for creating highly stretchable 3D-architected conductors. We show that 3D architectures can facilitate the design of soft conductors in three aspects: (1) enhancing the overall stretchability by harnessing the architecture geometries, (2) reducing the overall density, (3) enabling conformal contact with curved solids and sensing their large deformation, and (4) enlarging contact areas with engineering fluids and sensing the fluid compositions. We expect that this 3D-architected design of soft conductors with high stretchability, low density, tunable porosity and acute sensitivity may open promising avenues for broad applications in soft and wet environments, including healthcare devices,[16] quality monitoring and treatment of water,[34] human-interface dampers and absorbents,[35] soft robotics,[36] and tissue scaffolds.[37]

2. Methods

The strategy integrates two sets of mechanisms: design of elastomer lattice structures (Fig. 1a and e–g) and conformal coating of conductive hydrogels (Fig. 1b–d, h and i). First, we design and fabricate elastomer lattices with highly complex architectures (Fig. 1a). The fabrication challenge comes from the suspending beams in the structures (Fig. 1a). Direct manufacturing with nozzle-based direct-writing,[33,38–40] photopolymerization-based stereolithography[24,41,42] or polyjet printing[43,44] is unable to accomplish the fabrication. To enable the fabrication, we employ a method so-called "indirect additive manufacturing"

Sonny Astani Department of Civil and Environmental Engineering, University of Southern California, Los Angeles, CA 90089, USA.
E-mail: qimingw@usc.edu

† Electronic supplementary information (ESI) available. See DOI: 10.1039/c7sm01435j

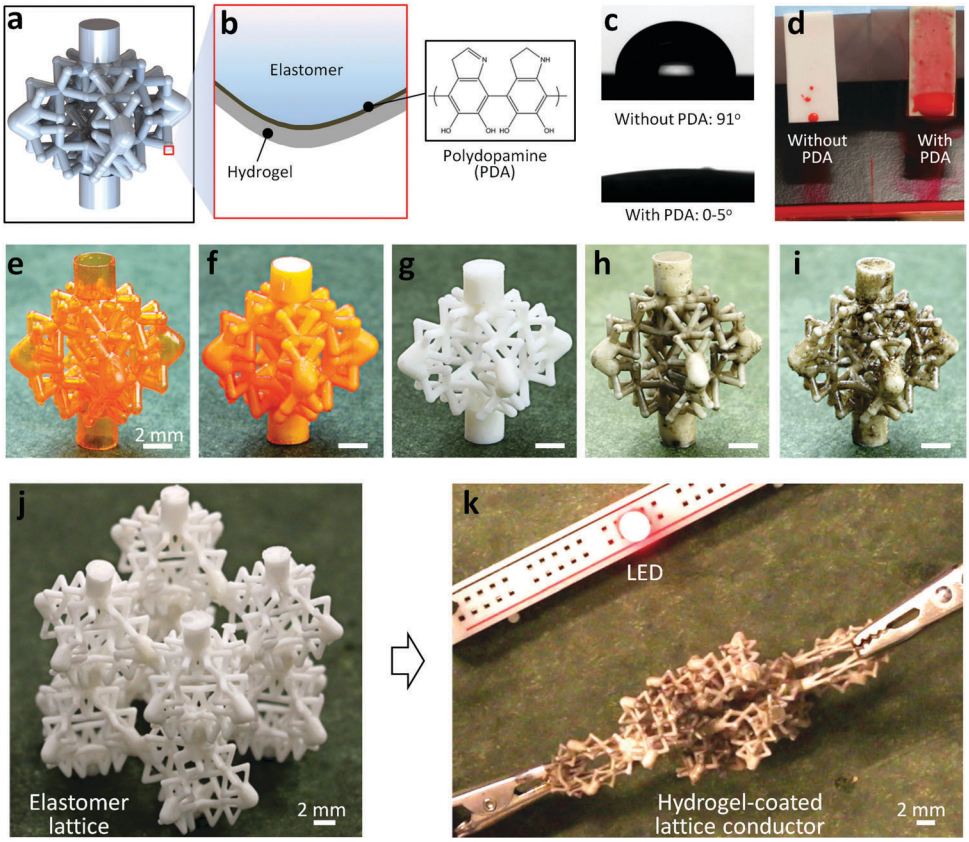

Fig. 1 Design and fabrication of lattice conductors. (a) A model of unit cell structures. (b) A schematic to show the hydrogel-elastomer laminate. (c) Contact angles of a poly(acrylamide) hydrogel pre-solution droplet on elastomer surfaces without or with polydopamine (PDA) coatings. (d) Dyed hydrogel pre-solutions coated on tilted elastomer surfaces without or with PDA coatings. (e–i) Sample fabrication process: (e) 3D printed water dissolvable scaffold, (f) elastomer cured within the scaffold channels, (g) free-standing elastomer structure after scaffold dissolution, (h) PDA conformally coated on the elastomer structure and (i) hydrogel conformally coated on the PDA coating. (j) Large-scale elastomer lattice. (k) Deformed large-scale lattice conductor that is conductive to lighten an LED.

by utilizing a water-soluble supporting scaffold (Fig. 1e–g and Fig. S1, ESI†).[45–47] The fabrication method can achieve resolution as low as 150 μm (beam diameter). Not only unit cell structures (Fig. 1g), can the method product large-scale lattices with a number of unit cells with total sample size as large as ~5 cm (Fig. 1j).

Then, we conformally coat an ion-doped conductive hydrogel layer around the elastomer lattice beams (Fig. 1a–d). It is challenging to conformally coat water-containing hydrogel pre-solutions on the hydrophobic elastomer surface (Fig. 1c and d). To enable the coating, UV or Ozone assisted chemical anchoring has been employed by other researchers.[29,48,49] Although the chemical anchoring method works well for elastomers with planar or slightly curved surfaces, it is challenging for the complexly architected lattices with complex internal surfaces.[50] To enable the conformal coating, we first dip-coat a polydopamine (PDA) interfacial layer (40–60 nm) around the elastomer beams (Fig. 1b–d, h and Fig. S2, ESI†), followed by an ion-doped poly(acrylamide) hydrogel coating (Fig. 1i).[50] PDA layer has both catechol and amine groups within its molecular structure and can form strong covalent and non-covalent interactions with a wide range of material surfaces, both hydrophobic and hydrophilic;[51,52] therefore, hydrogel layer can be conformally coated upon the PDA-coated elastomer structures (Fig. 1c, d and i). The coating thickness of the hydrogel can be controlled by varying the concentrations of the crosslinking agents and accelerators, achieving thickness ranging from 5 to 300 μm (Fig. S3, ESI†). Since the ion-doped hydrogel is conductive and stretchable, the hydrogel-coated lattice conductors are conductive to AC voltages under large stretches (Fig. 1k).

3. Results and discussions

Effect of 3D architectures on the stretchability

Fractal cuts have been proved to be a good strategy to enhance the overall stretchability of 2D structures.[20,22,53–57] Park *et al.* demonstrated that partitioning a 3D solid into islands connected by small soft ligands can significantly enhance the over stretchability.[58,59] Here, we move one step further and hypothesize that 3D fractal architectures can be harnessed to enhance the structural stretchability of soft conductors. To test this hypothesis, we fabricate a series of lattice conductors in self-similar fractal octahedron architectures (Fig. 2a). Uniaxial stretching tests show

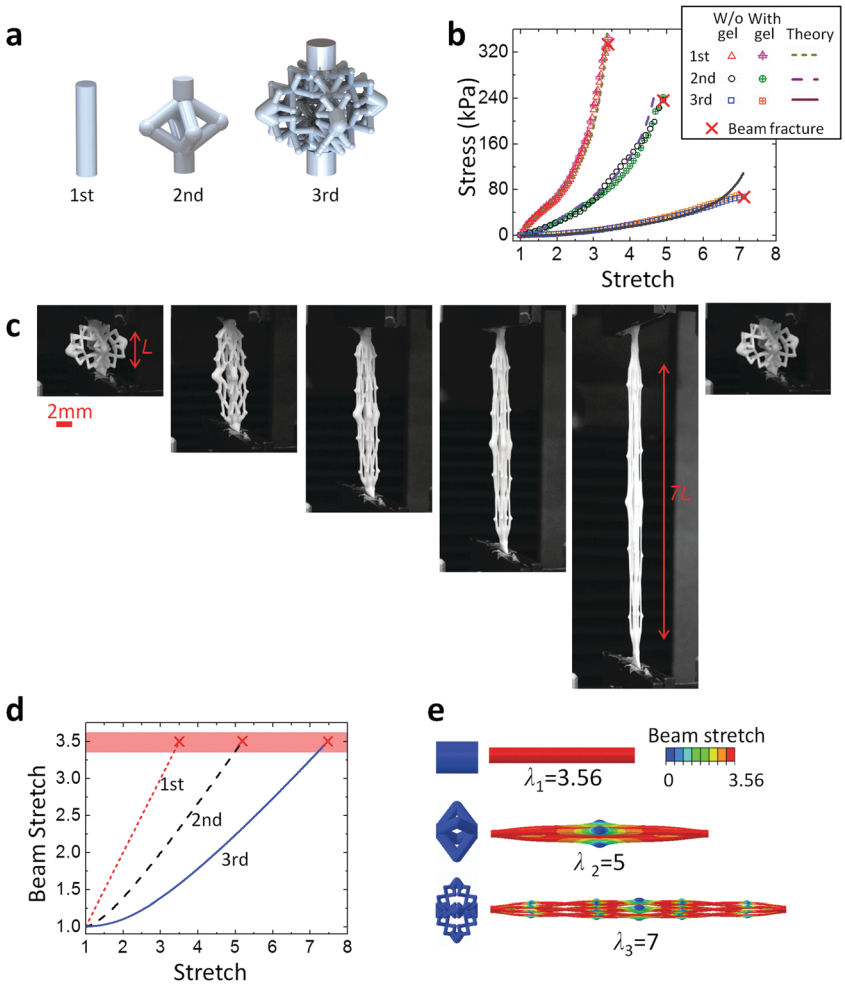

Fig. 2 Stretchability of Lattice conductors. (a) The CAD models of unit structures at various fractal orders. (b) Experimentally measured and theoretically predicted nominal stresses of various elastomer lattices and hydrogel-coated lattice conductors in functions of applied uniaxial stretches. (c) Image sequences to show cyclic stretching of the third order elastomer lattice. (d) Theoretically predicted beam strains in various elastomer structures in functions of applied uniaxial stretches. The red shaded area illustrates the failure of the elastomer beams. (e) Finite element analyses of various elastomer structures to show the beam stretches.

that the stretchability of the lattices increases with the fractal orders (Fig. 2b, c and Movie S1, ESI†). The maximum stretch of the first order structure is 3.5, while those of the second and third order lattice conductors are around 5 and 7.1, respectively (Fig. 2b). The stretchability of the third order lattice conductors is twice of that of the first order. It is noted that small extra segments are designed on the structures to enable easy clamping of the structures during the mechanical testing (Fig. 2a); we neglect the effect of these segments on the failure behaviors because we try to clamp the whole extra segments during the mechanical testing. Qualitatively, the improvement of stretchability is because that the architected beams with varied tilted angles need to be first aligned along the stretching direction and then elongated with the stretching. The alignment delays the stretching in individual beams. The similar stretch-delaying effect can be found in tendons where the mechanical stretching first unfolds and aligns the randomly orientated or crimped fibers.[60] It is noted that the stretchability and stress-stretch behaviors of the lattice conductors and elastomer lattices almost coincide (Fig. 2b), primarily because the modulus and thickness of the hydrogel (0.4–1 kPa, 30–50 μm in thickness, Fig. S4, ESI†) are much smaller than those of the elastomer (~30–300 kPa, 300–1000 μm in diameter).

To quantitatively understand the stretchability of the fractal lattice conductors, we develop an analytical model as follows. For the second-order structure under uniaxial stretch λ_2 (Fig. 2a), the axial stretch of the beam is $\lambda_{2,1}$ and the stretch in the lateral direction is λ_2^{α}, where α indicates the compressibility of the structure ($-0.5 \leq \alpha < 0$). Through a geometric analysis in the octahedron architecture (similar as the eight-chain model[61]), we can approximate the uniaxial stretch of the octahedron beam as

$$\lambda_{2,1}(\lambda_2) = \sqrt{\frac{{\lambda_2}^{2(1+\varsigma)} + 2{\lambda_2}^{2\alpha}}{3}} \quad (1)$$

where a very small parameter ς ($\ll 1$) is used to enforce the accuracy of the model. For the third order structure under

uniaxial stretch λ_3 (Fig. 2a), we further denote the uniaxial stretch of the elastomer beam as $\lambda_{3,1}$. Following a similar geometrical analysis, we can formulate $\lambda_{3,1}$ as

$$\lambda_{3,1}(\lambda_3) = \sqrt{\frac{\left(\sqrt{\frac{\lambda_3^{2(1+\varsigma)} + 2\lambda_3^{2\alpha}}{3}}\right)^{2(1+\varsigma)} + 2\left(\sqrt{\frac{\lambda_3^{2(1+\varsigma)} + 2\lambda_3^{2\alpha}}{3}}\right)^{2\alpha}}{3}} \quad (2)$$

Through analyzing the stress-stretch behaviors of the lattice conductors, we can obtain the parameters $\varsigma \approx 0.08$ and $\alpha \approx -0.33$ (theoretical predictions shown in Fig. 2b, the model described in ESI† and Fig. S5 and S6). Using eqn (1)–(2), we plot the theoretically predicted beam stretches in functions of the overall stretches on the structures at various orders in Fig. 2d. As shown in Fig. 2d, the fractal architectures can significantly delay the beam stretch: as the failure stretch of the elastomer beam is 3.5, the beam stretch of the second order structure fails when the overall stretch $\sim$5.2, while the third order $\sim$7.3. These theoretical predictions are consistent with the experimental observations (Fig. 2c). We further develop finite element models to calculate the beam stretches of the lattice structures under varied overall stretches (Fig. 2e). The numerical results can also roughly agree with the experimentally observed results (Fig. 2e).

Effect of 3D architectures on the density

It is highly desirable for the future electronics to feature low density to enable easy portability, and high stretchability along with skin-like rigidity to enable better interfacing with the human.[7–9] To illustrate these features, we construct stretchability-density and rigidity-density Ashby charts in Fig. 3. The relative density of the lattice conductor can be written as

$$\frac{\rho}{\rho_0} = \left(\frac{3\sqrt{3}\pi d^2}{4l^2}\right)^{i-1} \quad (3)$$

where ρ is the effective density of the lattice conductor and ρ_0 is the density of the elastomer ($\sim$1 g cm^{-3}), i is the fractal order number, d is the beam diameter and l is the beam length. The densities of the second order lattices are estimated as 0.09–0.5 g cm^{-3} and those of the third order lattices 0.008–0.02 g cm^{-3}. Compared to other 3D-architected conductors, the densities of the third order lattices are only slightly higher than the hollow metallic micro/nano lattices[41,42,62,63] (Fig. 3a). However, the stretchability of the current lattices is around 30 times of that of hollow metallic lattices, and at least twice of that of existing most stretchable conductors with 3D lattice architectures[33,58,64] (Fig. 3a).

In addition, the lattice architectures can also enable control of effective stiffness of the lattice conductors over a large range. Since the lattice architectures (*i.e.*, octahedron) follow a bending-dominant character, the effective relative Young's moduli of the lattice conductors should roughly follow a quadratic relationship with the relative density as[35,65]

$$\frac{E}{E_0} \approx \left(\frac{\rho}{\rho_0}\right)^2 = \left(\frac{3\sqrt{3}\pi d^2}{4l^2}\right)^{2(i-1)} \quad (4)$$

where E is the effective Youngs' modulus of the lattice conductor, E_0 is the modulus of the elastic beam (90–900 kPa). The fractal lattice design can enable the relative density to span over a large range from 0.008 to 0.4; therefore, the relative Youngs' moduli span over 4 orders of magnitude from 6.4×10^{-5} to 1.6×10^{-1}. As shown in Fig. 3b, the measured Young's moduli of the fabricated lattice conductors span from 6×10^{-1} to 3×10^{2} kPa with a nearly quadratic relationship $E/E_0 \approx (\rho/\rho_0)^{2.02}$. In addition, the effective moduli of the lattice conductors are within the modulus range of human skins and tissues (shaded area in Fig. 3b), thus expecting good adaption with human surfaces from the mechanical perspective.[66]

Effect of 3D architectures on the interactions with engineering solids

Next, we show that the 3D architectures can facilitate the lattice conductors to interact well with engineering solids. When a soft conductor interacts with an engineering solid, the interaction deformation between these two objects can usually exhibit

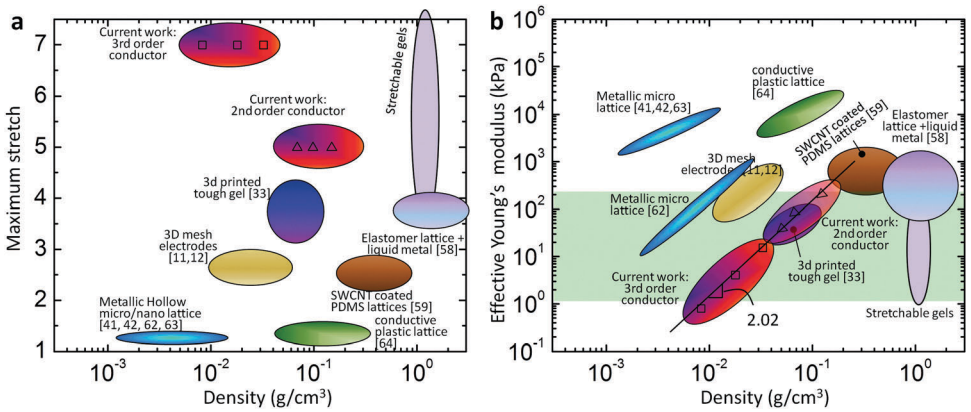

Fig. 3 Ashby charts to illustrate the mechanical properties of the lattice conductors. (a) Stretchability-density Ashby chart and (b) rigidity-density Ashby chart of existing 3D-architected conductors. The numbers in the square brackets are the reference numbers. The shaded area in (b) shows the modulus range of human tissues and skins.[66]

digital information through the conductivity change of the conductor. Most of existing stretchable sensors are in 2D planar configurations;[7] to monitor 3D large deformation, they are usually required to be attached to curved surfaces with special bonding treatments and spatial connections.[12,16,22,67] However, our 3D-architected lattice conductor can be used to monitor 3D large deformation of curved solids without special attachment on the curved surfaces.

We first show that the lattice conductors can remain highly conductive under large cyclic stretches (Fig. 4a and b). As shown in Fig. 4b, the third order lattice conductors can be reversibly stretched to stretch ~7 for more than 20 cycles, and the corresponding conductivities remain nearly constant for stretch 1 and 7, respectively (Fig. S7, ESI†). Within stretch 1–7, the structural resistances at various orders increase with the uniaxial stretches (Fig. 4c). The resistance-stretch relationship can be quantitatively understood as follows. If we assume the resistivity remains constant, the resistance of the stretched first-order conductor can be estimated as[25,26]

$$\frac{R}{R_0} = \lambda_1^2 \tag{5}$$

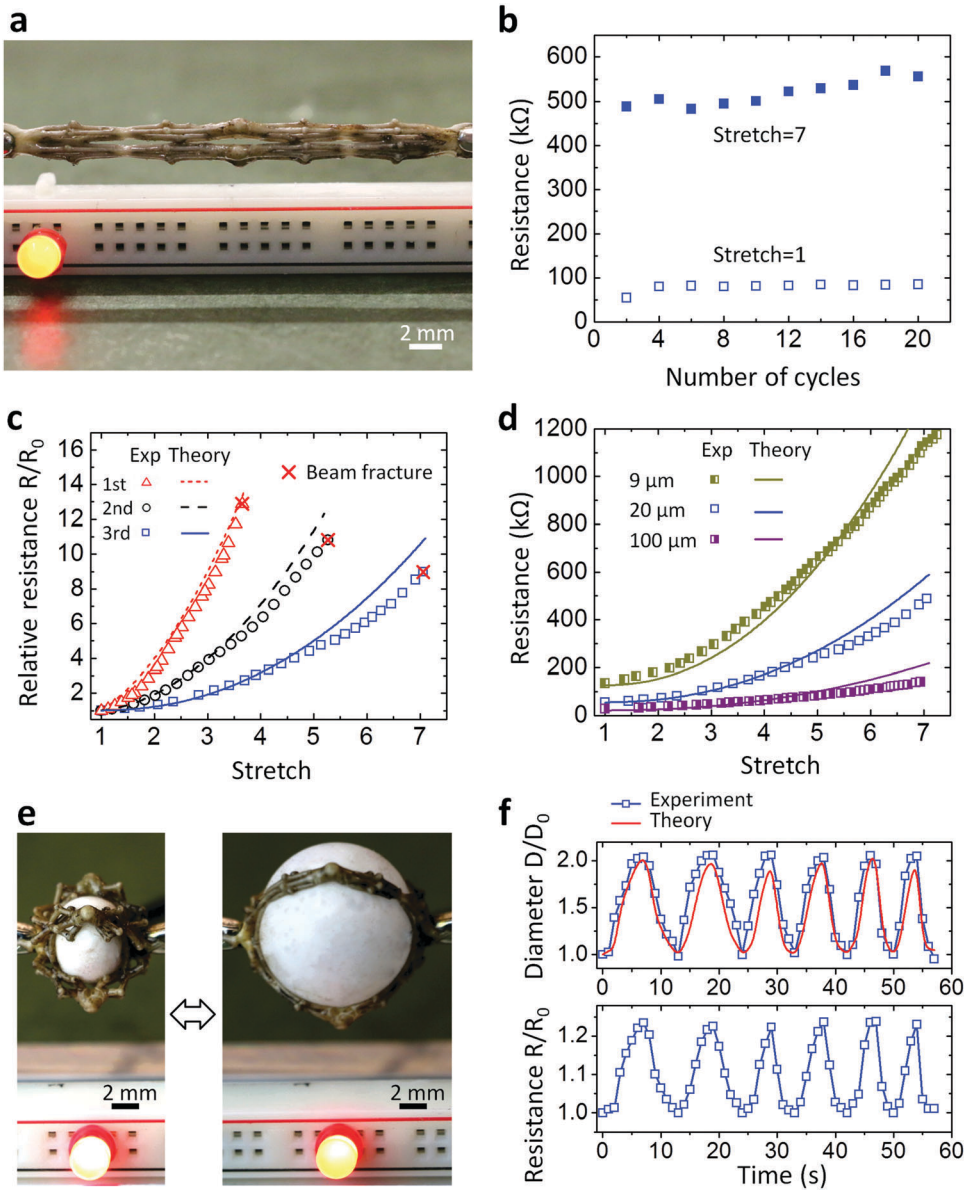

Fig. 4 Conductivity properties of lattice conductors under large stretches. (a) Stretched lattice conductor. (b) The resistance of the lattice conductor during 20 cycles of stretching between stretch 1 and 7. (c) Experimentally measured and theoretically predicted relative resistances of various lattice conductors in functions of applied uniaxial stretches. R_0 represents the resistance at undeformed state. (d) The resistances of the lattice conductors with various hydrogel thicknesses. The effective resistivities of the lattice conductors at the undeformed state can be estimated as 1.02×10^3 Ω m for 9 μm, 4.08×10^2 Ω m for 20 μm and 2.17×10^2 Ω m for 100 μm, respectively. (e) A cyclically expanding balloon is encapsulated within a lattice conductor. (f) The cyclically varying relative resistances of the lattice conductor and relative diameters of the balloon.

where R_0 is the resistance for $\lambda_1 = 1$. According to eqn (1) and (2), we can express the resistance for the second and third order lattice conductors as

$$\frac{R}{R_0} \approx \frac{\lambda_2^{2(1+\varsigma)} + 2\lambda_2^{2\alpha}}{3} \tag{6}$$

$$\frac{R}{R_0} \approx \frac{\left(\sqrt{\frac{\lambda_3^{2(1+\varsigma)} + 2\lambda_3^{2\alpha}}{3}}\right)^{2(1+\varsigma)} + 2\left(\sqrt{\frac{\lambda_3^{2(1+\varsigma)} + 2\lambda_3^{2\alpha}}{3}}\right)^{2\alpha}}{3} \tag{7}$$

where R_0 is the resistance for $\lambda_2 = 1$ and $\lambda_3 = 1$, respectively. It is noted that we here ignored the clamping segments outside of the main octahedron architectures. The predicted conductivities from eqn (5)–(7) match consistently with the measured conductivities of the lattice conductors at various orders (Fig. 4c). To further validate the theoretical predictions, we measure the conductivities of lattice conductors with varied thicknesses of hydrogel coatings, and the measured results are also roughly consistent with the theoretical predictions (Fig. 4d). The discrepancy between the theoretical and experimental results is probably due to the thickness inhomogeneity of the hydrogel coatings.

Then we demonstrate a 3D resistive sensor to monitor 3D large deformation of a curved solid. The essential goal of this demonstration is to use the 3D lattice conductors to monitor the beating of a heart *in vitro*.[68] We employ a cyclically deforming balloon to mimic the beating heart and encapsulate it with a lattice conductor, followed by measuring the conductivity on two ends of the lattice conductor (Fig. 3e, Fig. S8 and Movie S2, ESI†). As the balloon is deforming, the 3D lattice structure with low stiffness and high deformability can conformally deform around the balloon surface. Therefore, the stretch of the third order lattice conductor can be estimated as $\lambda_3 \approx D/D_0$, where D and D_0 are the diameters of the balloon at the deformed and initial state, respectively. Similar to eqn (7), the relative resistance can be estimated as

$$\frac{R}{R_0} \approx \frac{\left(\sqrt{\frac{(D/D_0)^{2(1+\varsigma)} + 2(D/D_0)^2}{3}}\right)^{2(1+\varsigma)} + 2\left(\sqrt{\frac{(D/D_0)^{2(1+\varsigma)} + 2(D/D_0)^2}{3}}\right)^{2\alpha}}{3} \tag{8}$$

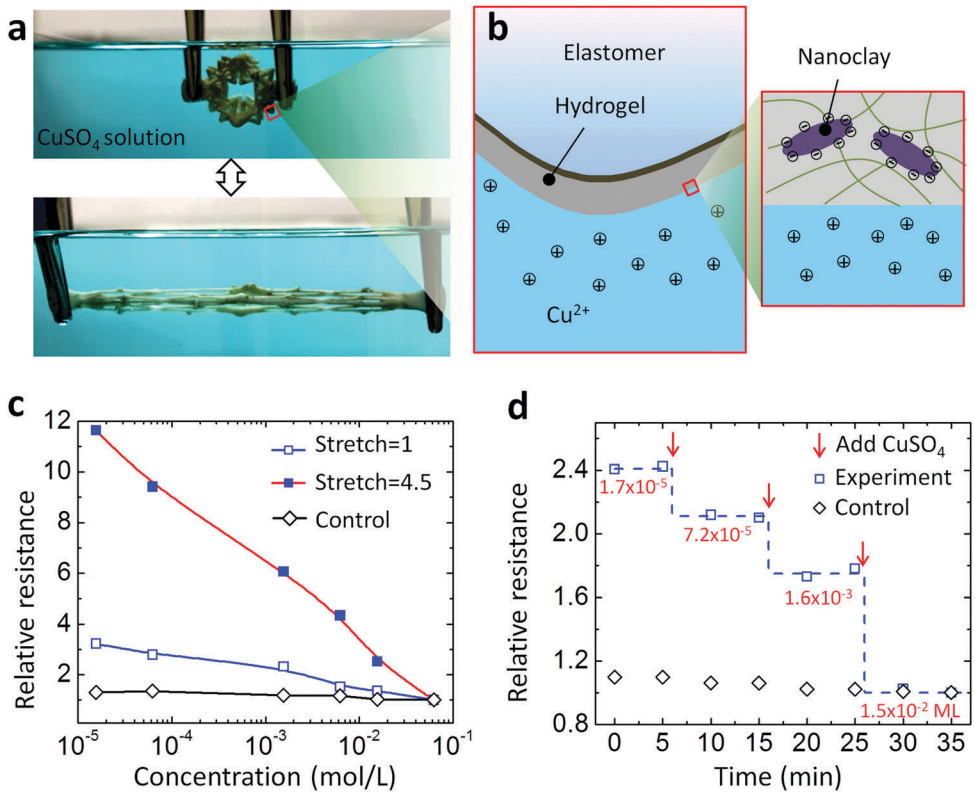

Fig. 5 Wastewater monitoring with lattice conductors. (a) A clamped lattice conductor immersed in a $CuSO_4$ solution and under cyclic stretching. (b) Schematics to show the nanoclay-embedded hydrogel on the lattice structure capable of adsorbing heavy metal ions. (c) The relative resistances (R/R^*) of the unstretched and stretched lattice conductors in functions of Cu^{2+} concentrations. R^* represents the resistance for the concentration 0.06 mol L^{-1}. The control results are the relative resistances of $CuSO_4$ solutions. (d) The relative resistances of the lattice conductor that adsorbs Cu^{2+} in a solution with step-increasing of Cu^{2+} concentrations. The red numbers in (d) represent the Cu^{2+} concentrations (mol L^{-1}). The resistance measurement is performed when the structure is taken out of the solution with the residue water removed.

with the measured resistances during the balloon actuation, we can theoretically calculate the balloon diameters (eqn (8)) which are consistent with the experimentally measured results (Fig. 4f).

Effect of 3D architectures on the interactions with engineering fluids

Besides the deformation-sensing capability, the 3D porous lattice conductors with hydrogel skins can be used to monitor heavy metal ions in the wastewater. Wastewater with heavy metal ions should be carefully treated before discharging into the environment because heavy metals are carcinogenic after long-term accumulation in living organisms.[34,69] The variation of the metal ion concentration can usually be monitored by conductivity measurements; however, the measurements have low sensitivity when the concentration is low ($<10^{-4}$ mol L^{-1}).[34] Here, we employ hydrogel-coated lattice conductors to monitor metal ion concentrations with higher sensitivity (Fig. 5a). Within the hydrogel, we embed negatively-charged nanoclay particles that promote the absorption of Cu^{2+} ions through electrostatic attractions (Fig. 5b).[34,70] And the absorption of Cu^{2+} can enhance the conductivities of the hydrogel-coated lattice conductors (Fig. 5c). In contrast to the direct conductivity measurement in the Cu^{2+} solution, we use a hydrogel layer to first absorb and accumulate Cu^{2+} within a hydrogel matrix. Therefore, the hydrogel absorption skin can significantly enhance the measurement sensitivity at the low concentration range (Fig. 5c). It is noted that to eliminate the effect of gel swelling we pre-swell the hydrogel layers in the DI water before the experiments (see ESI†). In addition, the porous character of the lattice structures enlarges the contact areas between the Cu^{2+} ions and hydrogels (Fig. 5a). Furthermore, cyclic large-strain stretching of the hydrogel-elastomer structure can also facilitate the mixing of the solution and the diffusion of heavy metal ions into the hydrogel layers (Fig. 5a).

To demonstrate the monitoring capability of the lattice conductors, we step-by-step increase the Cu^{2+} concentration in a $CuSO_4$ solution bath and measure the resistance of the lattice conductor after $\sim$5 min absorption. The measurement is carried out when the lattice conductors are taken out of the solution, and the water residue is removed (see ESI†). The measured resistances show step-wise decreasing with large resistance changes; however, direct measurement of the solution resistance only shows small resistance changes (Fig. 5d). It is noted that the required absorption time for thin gel layer (30 μm) is relatively short (only in several minutes) to enable time-effective sensing. The equilibrium absorption time scales with h^2/η where h is the hydrogel thickness and η is the diffusivity ($\sim 10^{-11}$ m^2 s^{-1} [34,69]). The equilibrium absorption time for 1 mm-thick hydrogel is estimated as 27.8 h, but only 1.5 min for 30 μm-thick hydrogels.

4. Conclusion

We recently reported carbon-grease-filled lattice conductors that are 3D-architected and stretchable.[46] Compared to the reported conductors, the current lattice conductors involve ionically conductive hydrogels conformally on the lattice surfaces, thus offering a special opportunity for interacting with the external environment. Although the hydrogels on the outer surfaces may require humidity control to maintain their properties in the long term,[29] the interactions with the external engineering objects can enable applications that have not been achieved by existing 3D-architected conductors,[11–21] such as sensing of the large deformation of curved solids and rapid wastewater monitoring (Fig. 4 and 5).

In summary, we report a type of stretchable 3D-architected lattice conductors. Besides the high stretchability and low density, the lattice conductors show great adaption when interfacing with engineering solids and fluids. With integrated features of high stretchability, 3D architecture, high porosity and low density, the designed lattice conductors may inspire a number of future research directions and applications. For example, 3D-architected metamaterials with the potent capability of tuning material properties by harnessing the structural architectures can be applied to design unconventional electronics with both controlled electronic conductivity and desirable mechanical performance.[19,64] In addition, with their skin-like rigidity, these hydrogel-based lattice conductors probably can be easily translated to a number of biomedical applications which require biocompatible electrodes with desirable shapes.[11,12,16]

Conflicts of interest

There are no conflicts to declare.

Acknowledgements

The research was funded by NSF grant CMMI-1649093. We acknowledge Dr Malancha Gupta for allowing us to use the contact angle goniometer in her lab. The SEM images were taken from Center for Electron Microscopy and Microanalysis (CEMMA) at the University of Southern California.

References

1 N. Fleck, V. Deshpande and M. Ashby, *Proc. R. Soc. London, Ser. A*, 2010, **466**, 2495–2516.
2 L. Montemayor, V. Chernow and J. R. Greer, *MRS Bull.*, 2015, **40**, 1122–1129.
3 L. J. Gibson and M. F. Ashby, *Cellular solids: structure and properties*, Cambridge University Press, 1999.
4 L. J. Gibson, M. F. Ashby and B. A. Harley, *Cellular materials in nature and medicine*, Cambridge University Press, 2010.
5 B. Trimmer, J. A. Lewis, R. F. Shepherd and H. Lipson, *Soft Robotics*, 2015, **2**, 3–6.
6 R. L. Truby and J. A. Lewis, *Nature*, 2016, **540**, 371–378.
7 J. A. Rogers, T. Someya and Y. Huang, *Science*, 2010, **327**, 1603–1607.
8 D.-H. Kim, R. Ghaffari, N. Lu and J. A. Rogers, *Annu. Rev. Biomed. Eng.*, 2012, **14**, 113–128.

9 Y. L. Kong, M. K. Gupta, B. N. Johnson and M. C. McAlpine, *Nano Today*, 2016, **11**, 330–350.
10 S. Bauer, S. Bauer-Gogonea, I. Graz, M. Kaltenbrunner, C. Keplinger and R. Schwödiauer, *Adv. Mater.*, 2014, **26**, 149–162.
11 J. Dewire and H. Calkins, *Nat. Rev. Cardiol.*, 2010, **7**, 129–138.
12 J. Liu, C. Xie, X. Dai, L. Jin, W. Zhou and C. M. Lieber, *Proc. Natl. Acad. Sci. U. S. A.*, 2013, **110**, 6694–6699.
13 J. J. Adams, E. B. Duoss, T. F. Malkowski, M. J. Motala, B. Y. Ahn, R. G. Nuzzo, J. T. Bernhard and J. A. Lewis, *Adv. Mater.*, 2011, **23**, 1335–1340.
14 B. Y. Ahn, E. B. Duoss, M. J. Motala, X. Guo, S.-I. Park, Y. Xiong, J. Yoon, R. G. Nuzzo, J. A. Rogers and J. A. Lewis, *Science*, 2009, **323**, 1590–1593.
15 M. S. Mannoor, Z. Jiang, T. James, Y. L. Kong, K. A. Malatesta, W. O. Soboyejo, N. Verma, D. H. Gracias and M. C. McAlpine, *Nano Lett.*, 2013, **13**, 2634–2639.
16 D.-H. Kim, N. Lu, R. Ghaffari, Y.-S. Kim, S. P. Lee, L. Xu, J. Wu, R.-H. Kim, J. Song and Z. Liu, *Nat. Mater.*, 2011, **10**, 316–323.
17 H. C. Ko, M. P. Stoykovich, J. Song, V. Malyarchuk, W. M. Choi, C.-J. Yu, J. B. Geddes Iii, J. Xiao, S. Wang and Y. Huang, *Nature*, 2008, **454**, 748–753.
18 R.-H. Kim, D.-H. Kim, J. Xiao, B. H. Kim, S.-I. Park, B. Panilaitis, R. Ghaffari, J. Yao, M. Li and Z. Liu, *Nat. Mater.*, 2010, **9**, 929–937.
19 Z. Song, T. Ma, R. Tang, Q. Cheng, X. Wang, D. Krishnaraju, R. Panat, C. K. Chan, H. Yu and H. Jiang, *Nat. Commun.*, 2014, **5**, 3140.
20 Y. Cho, J.-H. Shin, A. Costa, T. A. Kim, V. Kunin, J. Li, S. Y. Lee, S. Yang, H. N. Han and I.-S. Choi, *Proc. Natl. Acad. Sci. U. S. A.*, 2014, **111**, 17390–17395.
21 C. Ladd, J. H. So, J. Muth and M. D. Dickey, *Adv. Mater.*, 2013, **25**, 5081–5085.
22 S. Xu, Y. Zhang, J. Cho, J. Lee, X. Huang, L. Jia, J. A. Fan, Y. Su, J. Su and H. Zhang, *Nat. Commun.*, 2013, **4**, 1543.
23 S. Xu, Z. Yan, K.-I. Jang, W. Huang, H. Fu, J. Kim, Z. Wei, M. Flavin, J. McCracken and R. Wang, *Science*, 2015, **347**, 154–159.
24 D. K. Patel, A. H. Sakhaei, M. Layani, B. Zhang, Q. Ge and S. Magdassi, *Adv. Mater.*, 2017, 1606000.
25 C. Keplinger, J.-Y. Sun, C. C. Foo, P. Rothemund, G. M. Whitesides and Z. Suo, *Science*, 2013, **341**, 984–987.
26 J. Y. Sun, C. Keplinger, G. M. Whitesides and Z. Suo, *Adv. Mater.*, 2014, **26**, 7608–7614.
27 C.-C. Kim, H.-H. Lee, K. H. Oh and J.-Y. Sun, *Science*, 2016, **353**, 682–687.
28 C. H. Yang, B. Chen, J. J. Lu, J. H. Yang, J. Zhou, Y. M. Chen and Z. Suo, *Extreme Mech. Lett.*, 2015, **3**, 59–65.
29 H. Yuk, T. Zhang, G. A. Parada, X. Liu and X. Zhao, *Nat. Commun.*, 2016, **7**, 12028.
30 Y. Y. Lee, H. Y. Kang, S. H. Gwon, G. M. Choi, S. M. Lim, J. Y. Sun and Y. C. Joo, *Adv. Mater.*, 2016, **28**, 1636–1643.
31 Y. Wang, C. Zhu, R. Pfattner, H. Yan, L. Jin, S. Chen, F. Molina-Lopez, F. Lissel, J. Liu, N. I. Rabiah, Z. Chen, J. W. Chung, C. Linder, M. F. Toney, B. Murmann and Z. Bao, *Sci. Adv.*, 2017, **3**, e1602076.
32 J. Xu, S. Wang, G.-J. N. Wang, C. Zhu, S. Luo, L. Jin, X. Gu, S. Chen, V. R. Feig, J. W. F. To, S. Rondeau-Gagné, J. Park, B. C. Schroeder, C. Lu, J. Y. Oh, Y. Wang, Y.-H. Kim, H. Yan, R. Sinclair, D. Zhou, G. Xue, B. Murmann, C. Linder, W. Cai, J. B.-H. Tok, J. W. Chung and Z. Bao, *Science*, 2017, **355**, 59–64.
33 S. Hong, D. Sycks, H. F. Chan, S. Lin, G. P. Lopez, F. Guilak, K. W. Leong and X. Zhao, *Adv. Mater.*, 2015, **27**, 4035–4040.
34 G. Jing, L. Wang, H. Yu, W. A. Amer and L. Zhang, *Colloids Surf., A*, 2013, **416**, 86–94.
35 L. J. Gibson and M. F. Ashby, *Cellular solids: structure and properties*, Cambridge University Press, 1997.
36 R. F. Shepherd, F. Ilievski, W. Choi, S. A. Morin, A. A. Stokes, A. D. Mazzeo, X. Chen, M. Wang and G. M. Whitesides, *Proc. Natl. Acad. Sci. U. S. A.*, 2011, **108**, 20400–20403.
37 S. V. Murphy and A. Atala, *Nat. Biotechnol.*, 2014, **32**, 773–785.
38 A. S. Gladman, E. A. Matsumoto, R. G. Nuzzo, L. Mahadevan and J. A. Lewis, *Nat. Mater.*, 2016, **15**, 413–418.
39 Z. Qin, B. G. Compton, J. A. Lewis and M. J. Buehler, *Nat. Commun.*, 2015, **6**, 7038.
40 S. Shan, S. H. Kang, J. R. Raney, P. Wang, L. Fang, F. Candido, J. A. Lewis and K. Bertoldi, *Adv. Mater.*, 2015, **27**, 4296–4301.
41 X. Zheng, H. Lee, T. H. Weisgraber, M. Shusteff, J. DeOtte, E. B. Duoss, J. D. Kuntz, M. M. Biener, Q. Ge and J. A. Jackson, *Science*, 2014, **344**, 1373–1377.
42 X. Zheng, W. Smith, J. Jackson, B. Moran, H. Cui, D. Chen, J. Ye, N. Fang, N. Rodriguez, T. Weisgraber and C. M. Spadaccini, *Nat. Mater.*, 2016, **15**, 1100–1106.
43 D. Rus and M. T. Tolley, *Nature*, 2015, **521**, 467–475.
44 N. W. Bartlett, M. T. Tolley, J. T. Overvelde, J. C. Weaver, B. Mosadegh, K. Bertoldi, G. M. Whitesides and R. J. Wood, *Science*, 2015, **349**, 161–165.
45 Q. Wang, J. A. Jackson, Q. Ge, J. B. Hopkins, C. M. Spadaccini and N. X. Fang, *Phys. Rev. Lett.*, 2016, **117**, 175901.
46 Y. Jiang and Q. Wang, *Sci. Rep.*, 2016, **6**, 34147.
47 R. Liska, F. Schwager, C. Maier, R. Cano-Vives and J. Stampfl, *J. Appl. Polym. Sci.*, 2005, **97**, 2286–2298.
48 H. Yuk, T. Zhang, S. Lin, G. A. Parada and X. Zhao, *Nat. Mater.*, 2016, **15**, 190–196.
49 J. Kim, J. Yoon and R. C. Hayward, *Nat. Mater.*, 2010, **9**, 159–164.
50 P. Le Floch, X. Yao, Q. Liu, Z. Wang, G. Nian, Y. Sun, L. Jia and Z. Suo, *ACS Appl. Mater. Interfaces*, 2017.
51 H. Lee, S. M. Dellatore, W. M. Miller and P. B. Messersmith, *Science*, 2007, **318**, 426–430.
52 S. Hong, Y. S. Na, S. Choi, I. T. Song, W. Y. Kim and H. Lee, *Adv. Funct. Mater.*, 2012, **22**, 4711–4717.
53 S. Yang, I.-S. Choi and R. D. Kamien, *MRS Bull.*, 2016, **41**, 130–138.
54 Y. Tang, G. Lin, L. Han, S. Qiu, S. Yang and J. Yin, *Adv. Mater.*, 2015, **27**, 7181–7190.
55 K.-I. Jang, H. U. Chung, S. Xu, C. H. Lee, H. Luan, J. Jeong, H. Cheng, G.-T. Kim, S. Y. Han, J. W. Lee, J. Kim, M. Cho, F. Miao, Y. Yang, H. N. Jung, M. Flavin, H. Liu, G. W. Kong,

K. J. Yu, S. I. Rhee, J. Chung, B. Kim, J. W. Kwak, M. H. Yun, J. Y. Kim, Y. M. Song, U. Paik, Y. Zhang, Y. Huang and J. A. Rogers, *Nat. Commun.*, 2015, **6**, 6566.

56 J. A. Fan, W.-H. Yeo, Y. Su, Y. Hattori, W. Lee, S.-Y. Jung, Y. Zhang, Z. Liu, H. Cheng and L. Falgout, *Nat. Commun.*, 2014, **5**, 3266.

57 T. C. Shyu, P. F. Damasceno, P. M. Dodd, A. Lamoureux, L. Xu, M. Shlian, M. Shtein, S. C. Glotzer and N. A. Kotov, *Nat. Mater.*, 2015, **14**, 785–789.

58 J. Park, S. Wang, M. Li, C. Ahn, J. K. Hyun, D. S. Kim, D. K. Kim, J. A. Rogers, Y. Huang and S. Jeon, *Nat. Commun.*, 2012, **3**, 916.

59 D. Cho, J. Park, J. Kim, T. Kim, J. Kim, I. Park and S. Jeon, *ACS Appl. Mater. Interfaces*, 2017, **9**, 17369–17378.

60 J. F. Vincent, *Structural biomaterials*, Princeton University Press, Princeton, 2012.

61 E. M. Arruda and M. C. Boyce, *J. Mech. Phys. Solids*, 1993, **41**, 389–412.

62 T. A. Schaedler, A. J. Jacobsen, A. Torrents, A. E. Sorensen, J. Lian, J. R. Greer, L. Valdevit and W. B. Carter, *Science*, 2011, **334**, 962–965.

63 C. Xu, B. M. Gallant, P. U. Wunderlich, T. Lohmann and J. R. Greer, *ACS Nano*, 2015, **9**, 5876–5883.

64 E. Fantino, A. Chiappone, I. Roppolo, D. Manfredi, R. Bongiovanni, C. F. Pirri and F. Calignano, *Adv. Mater.*, 2016, **28**, 3712–3717.

65 V. Deshpande, M. Ashby and N. Fleck, *Acta Mater.*, 2001, **49**, 1035–1040.

66 Y.-C. Fung, *Biomechanics: mechanical properties of living tissues*, Springer Science & Business Media, 2013.

67 G. Lanzara, N. Salowitz, Z. Guo and F. K. Chang, *Adv. Mater.*, 2010, **22**, 4643–4648.

68 E. T. Roche, M. A. Horvath, I. Wamala, A. Alazmani, S.-E. Song, W. Whyte, Z. Machaidze, C. J. Payne, J. C. Weaver, G. Fishbein, J. Kuebler, N. V. Vasilyev, D. J. Mooney, F. A. Pigula and C. J. Walsh, *Sci. Transl. Med.*, 2017, **9**.

69 K. Yamashita, T. Nishimura and M. Nango, *Polym. Adv. Technol.*, 2003, **14**, 189–194.

70 M. Kurecic and M. S. Smole, *Polymer nanocomposite hydrogels for water purification*, INTECH Open Access Publisher, 2012.

Supporting Information

Stretchable 3D Lattice Conductors

Tingyao Li, Yanhui Jiang, Kunhao Yu, Qiming Wang*
Sonny Astani Department of Civil and Environmental Engineering, University of Southern California, Los Angeles, CA 90089, USA.
*E-mail: qimingw@usc.edu

1. Experimental procedure

Fabrication of lattice conductors: We use a projection microstereolithography system to fabricate water-soluble hollow scaffolds. The printing process has been reported elsewhere and outlined in **Fig. S1** [1, 2]. Once dried with air for 2 min (**Fig. 1e**), the hollow scaffold is filled with tin-catalyzed silicone elastomers (mold max NV14, base:crosslinker=100:7 by weight, Smooth-on). The filled elastomers are cured for 12 h at 25 ^{o}C (**Fig. 1f**). After that, the structure is immerged in 1 mol/L NaOH solution for 4 h. The elastomer structures are ready after washing in DI water for 2 min and air-drying for 2 min (**Fig. 1g**). Then, the elastomer lattices are dipped in a mixture of dopamine (2 mg/mL, Sigma-Aldrich) and 10 mM Tris-HCl (pH 8.5, bioWorld) for overnight. After the dipping, the elastomer lattice is rinsed with water and dried with nitrogen for 2 min. We then make a hydrogel pre-solution by mixing 2.34g acrylamide (Sigma-Aldrich), 0.006g N,N-methylenebisacrylamide (Sigma-Aldrich), various grams ammonium persulfate (APS, Sigma-Aldrich), 22.5 ml DI water as a solvent, 7.5 ml Glycerol (Sigma-Aldrich) and 6 g NaCl. Once adding 0.08 ml N,N,N',N'-tetramethylethylenediamine (TEMED, Sigma-Aldrich)[3], we record the time. At various time points, the elastomer structures are dipped into the hydrogel pre-solution for five seconds. The coated structures are baked in an oven at 60^{o} for 30 min, followed by UV irradiation (8W, 254 nm) for 20 min. The manufacturing throughput is estimated as 4.47 mm^3/min. The thicknesses of the hydrogel coatings are measured using an optical microscope (Nikon ECLIPSE LV100ND) to image the cross sections of hydrogel-elastomer laminates (**Fig. S3**).

Mechanical characterization: The elastomer lattices and lattice conductors are cyclically stretched by an Instron tester with rate 0.0167 mm/s (model 5942, Instron). Finite element calculations are carried out in a commercial finite-element software, ABAQUS 6.10.1(**Fig. 2e**). The elastomer beams are taken to obey eight-chain model with parameters μ=30 kPa and n_1=2.9 (see **Eq. 2**)[4]. The models are discretized by C3D8R elements and the result accuracy is ascertained through mesh refinement studies. The loadings in the simulations are displacement-controlled.

Electrical characterization: The resistances of the lattice conductors are measured using four-point-probe method sourced by a 60 Hz AC voltage 5-28V[3, 5]. The LEDs are connected in series with the hydrogel-elastomer structures powered by the 60 Hz AC voltage (20V).

Expanding balloon: Similar to the fabrication of elastomer architectures, an elastomer balloon with diameter ~1.5 cm and wall-thickness 500 μm is fabricated based on a hollow water-dissolvable scaffold (**Fig. S8**). Once fabricated, the elastomer balloon is encapsulated within the third-order lattice conductor and activated by a controlled air pressure. The balloon diameter variation is measured from the image sequences. The resistances on two ends of the lattice conductors are measured using the four-point-probe method.

Wastewater monitoring: A lattice conductor with ~30μm hydrogel coating is first dipped in DI water for more than 2 hours to ensure equilibrium swelling of the hydrogel, and then dipped in the $CuSO_4$ solution for 5 min. Then the lattice conductor is taken out of the solution, and the residue water on the surface is quickly absorbed and removed by a tissue paper. The lattice conductor is subsequently mounted on a four-point-probe setup to measure the resistance. The resistance measurement only takes ~15s. Repeated measurements are conducted when the concentration of the $CuSO_4$ solution is increased step-by-step by adding concentrated $CuSO_4$ solutions.

2. Theoretical analysis of stress-strain behavior of the lattice conductors

Considering the geometrical deformation in **Eqs. 1-2**, we can formulate the free energy of the *i*th order lattice (**Fig. 2a**) as

$$W_i(\lambda_i) \approx \nu_i W_1(\lambda_{i,1}) \tag{S1}$$

where *i*=2 and 3, λ_i is the overall uniaxial stretch, $\lambda_{i,1}$ is the stretch of the smallest beam, $\nu_2 \approx 3\sqrt{3}\pi d^2/(4l^2)$ and $\nu_3 \approx 27\pi^2 d^4/(16l^4)$ are the volume fraction of the second and third order structure, d is the beam diameter and l is the beam length. The elastomer can be modeled using eight-chain model with the free energy density expressed as[4]

$$W_1(\lambda_1) = \mu n_1 \left(\frac{\beta_1}{\tanh \beta_1} + \ln \frac{\beta_1}{\sinh \beta_1} \right) \tag{S2}$$

where μ is the shear modulus of the hydrogel-elastomer hybrid, n_1 is the average Kuhn number of the polymer chains, $\beta_1 = \Gamma^{-1}\left(\sqrt{(\lambda_1^2 + 2\lambda_1^{-1})/(3n_1)} \right)$, λ_1 is the uniaxial stretch, $\Gamma^{-1}(\ )$ is the inverse Langevin function, and the Langevin function is written as $\Gamma(x) = \coth x - 1/x$.

The corresponding uniaxial nominal stress can be expressed as

$$s_i(\lambda_i) = \frac{\partial W_i(\lambda_i)}{\partial \lambda_i} \tag{S3}$$

where *i*=2 and 3. The theoretical predictions from **Eq. S3** can consistently match the stress-stretch behaviors of the lattice conductors at various orders using parameters μ≈30 kPa, n_1≈2.9, ς≈0.08 and α≈ -0.33 (**Fig. 2b**). It is noted that the compressibility α can be validated by experiments shown in **Fig. S6**. To further validate the theoretical model, we vary the beam aspect ratios *d/l* of the third order structures and

test their stress-strain behaviors which are also consistent with the theoretical predictions (**Fig. S5)**.

3. Supplementary figures

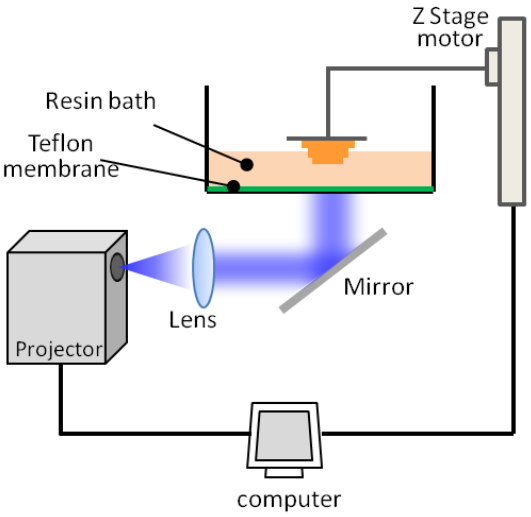

Figure S1. Schematic to show the 3D-printing process of the water-dissolvable scaffolds[2]. First, a 3D hollow computer-aided design (CAD) model is sliced into a series of images with a prescribed spacing along the vertical direction. These 2D slice images, illuminated with UV/blue light from a light emitting diode, are sequentially projected onto a resin bath, where the photoresin is capped in a prescribed height by a printing glass stage. The exposed resin is solidified, forming a layer structure bonded onto the printing stage. To eliminate the adhesion between the solidified resin and bath, an oxygen permeable membrane (Teflon fluoropolymer, CSHyde, USA) is attached on the bottom, inducing a thin layer (~5-20μm) of the oxygen-rich dead zone to quench the photopolymerization. As the printing stage is lifted off, the fresh resin can flow back. By lowering down the stage by a prescribed height and illuminating the resin with another slice image, the second layer can be printed and bonded onto the first layer. By repeating these processes, we can print a hollow scaffold with nearly arbitrary 3D architectures.

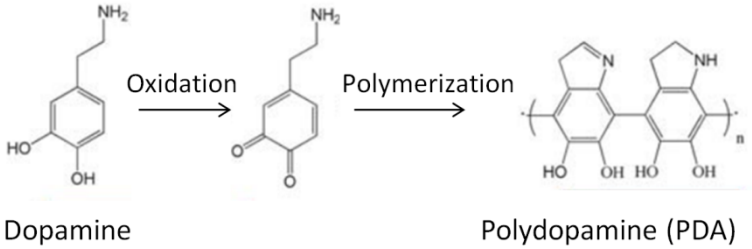

Figure S2. Dopamine molecules are oxidized in an acid solution and then polymerized overnight[6].

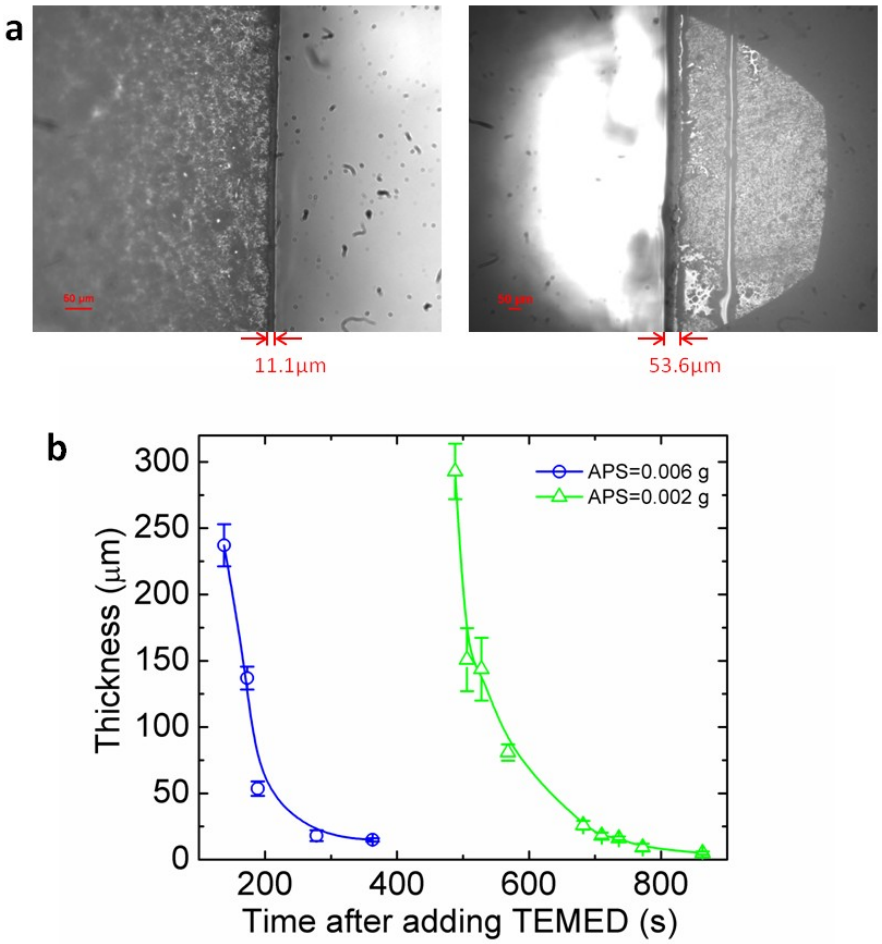

Figure S3. (a) Optical microscope images to show hydrogel layers with thickness 11.1 μm and 53.6 μm, respectively. (b) The thicknesses of hydrogel layers for various ammonium persulfate (APS, photoinitiator) concentrations and time after adding N,N,N',N'-tetramethylethylenediamine (TEMED, crosslinking accelerator). We dip-coated hydrogel layers on the elastomer structures at different time points after adding the crosslinking accelerator TEMED into the hydrogel pre-solution.

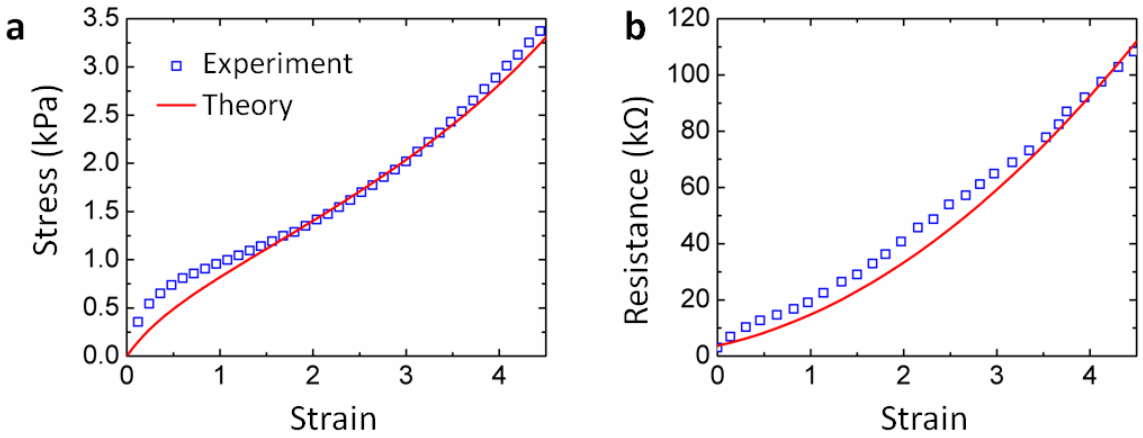

Figure S4. Experimentally measured and theoretically fitted (a) nominal stresses and (b) resistance of a hydrogel bar sample in functions of applied uniaxial strains. The theory for the stress-strain behavior follows **Eq. S2** with parameter shear modulus $\mu \approx 0.4$ kPa and $n_1 \approx 4$.

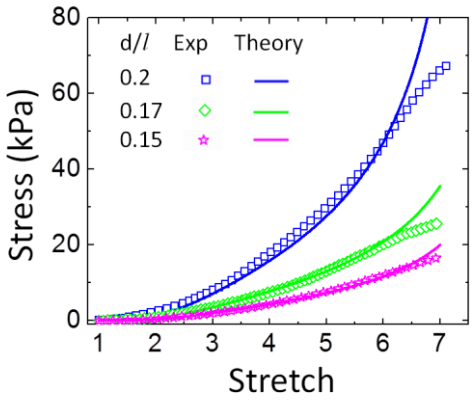

Figure S5. Experimentally measured and theoretically predicted stress-stretch behaviors of the third-order lattice with various beam aspect ratios.

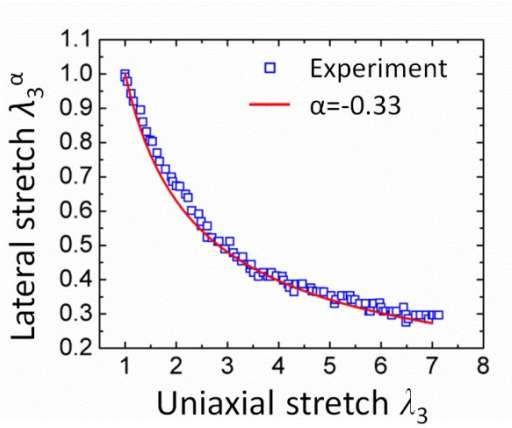

Figure S6. The lateral stretch in a function of the uniaxial stretch of the third-order lattice.

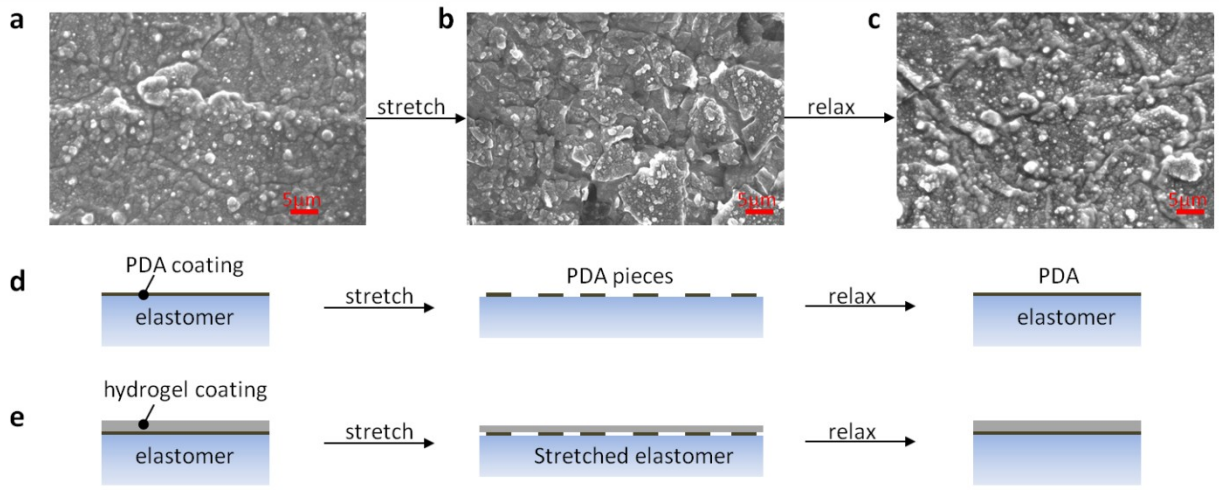

Figure S7. (a-c) SEM images of PDA coatings on a mold max elastomer substrate at (a) unstretched, (b) stretched and (c) relaxed states. (d) Schematics to show the PDA coating on an elastomer structures in various states. At the stretched state, the PDA coating is fractured into islands; however, due to high adhesion between the PDA and the elastomer, the PDA islands are reassembled into a PDA coating after relaxation. (e) Similarly, we expect a PDA interfacial layer sandwiched between a hydrogel layer and elastomer substrate should follow a similar behavior during the substrate stretching and relaxing. The non-debonding between the PDA and elastomer ensures a robust hydrogel coating with no mismatch with the underlying elastomers during the elastomer stretching and relaxation. Since the maximum stretch of the elastomer is 3.5 (**Fig. 2b**) and the maximum stretch of the hydrogel is more than 5 (**Fig. S4**), the hydrogel will remain intact before the elastomer failure.

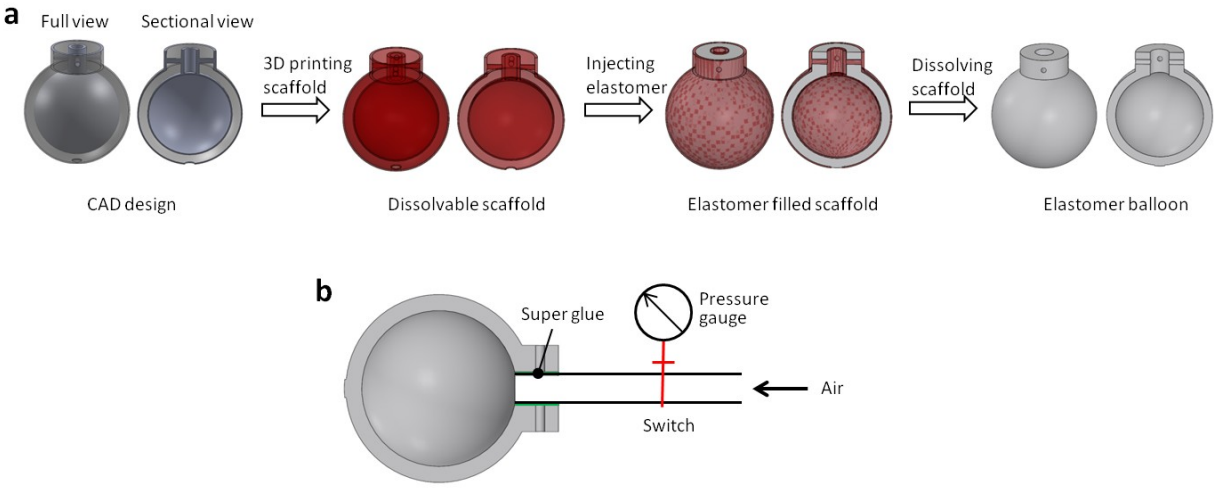

Figure S8. (a) The fabrication process of an elastomer balloon similar to the fabrication process of the elastomer structure shown in **Fig. 1e-i**. (b) Experimental setup for expanding the elastomer balloon.

4. Supplementary movies

Movie S1: Cyclical stretching of the third-order elastomer structure. The movie speed is 10 times of the real experiment. The stretch goes from 0 to 7, returns to 0 and then increases until beam fracture.

Movie S2: An elastomer heart-mimic encapsulated within a lattice conductor is expanding cyclically using air pressure (three cycles).

Reference

[1] Q. Wang, J. A. Jackson, Q. Ge, J. B. Hopkins, C. M. Spadaccini, N. X. Fang, Physical review letters 2016, 117, 175901.
[2] Y. Jiang, Q. Wang, Scientific reports 2016, 6, 34147.
[3] C. Keplinger, J.-Y. Sun, C. C. Foo, P. Rothemund, G. M. Whitesides, Z. Suo, Science 2013, 341, 984.
[4] E. M. Arruda, M. C. Boyce, Journal of the Mechanics and Physics of Solids 1993, 41, 389.
[5] H. Yuk, T. Zhang, S. Lin, G. A. Parada, X. Zhao, Nature materials 2016, 15, 190.
[6] H. Lee, S. M. Dellatore, W. M. Miller, P. B. Messersmith, Science 2007, 318, 426.